An Automated Approach to Magnetic Divertor Configuration Design

M. Blommaert[1], W. Dekeyser[2], M. Baelmans[2], N.R. Gauger[3] and D. Reiter[1]

[1] Institute of Energy and Climate research, Plasma physics (IEK-4), FZ Jülich GmbH, D-52425 Jülich, Germany

[2] KU Leuven, Department of Mechanical Engineering, Celestijnenlaan 300A, 3001 Leuven, Belgium

[3] RWTH Aachen University, Department of Mathematics and Center for Computational Engineering Science, Schinkelstr. 2, D-52062 Aachen, Germany

E-mail: `m.blommaert@fz-juelich.de`

Abstract.

Automated methods based on optimization can greatly assist computational engineering design in many areas. In this paper an optimization approach to the magnetic design of a nuclear fusion reactor divertor is proposed and applied to a tokamak edge magnetic configuration in a first feasibility study. The approach is based on reduced models for magnetic field and plasma edge, which are integrated with a grid generator into one sensitivity code. The design objective chosen here for demonstrative purposes is to spread the divertor target heat load as much as possible over the entire target area. Constraints on the separatrix position are introduced to eliminate physically irrelevant magnetic field configurations during the optimization cycle. A gradient projection method is used to ensure stable cost function evaluations during optimization. The concept is applied to a configuration with typical Joint European Torus (JET) parameters and it automatically provides plausible configurations with reduced heat load.

PACS numbers: 52.65.Kj, 52.65.Vv, 52.55.Rk,02.60.Pn

Keywords: divertor design, edge plasma modelling, magnetic topology, power deposition, sequential quadratic programming, parameter optimization.

1. Introduction

Tokamak divertors serve simultaneously for particle and heat exhaust from fusion reactors, making divertor design a challenging multi-physics task. A first design objective is to keep the heat load on the divertor plates below material limits, preventing excessive erosion and melting. For next step fusion reactors such as ITER [1] or power plants (Demo [2]), heat extraction is considered an even more severe design challenge. As a second design objective, plasma purity, in particular efficient helium ash removal, is to be ensured. Finally, a number of technical constraints have to be met.

An additional difficulty when designing the divertor configuration is that complex physical interactions between plasma, neutrals and solid materials govern these exhaust processes. Therefore designs are often based on involved numerical simulations, e.g. using the B2-Eirene plasma edge code system [3, 1]. Even on the most powerful supercomputers available today, divertor design is extremely CPU demanding, not least due to the large number of design variables and the complex convection-diffusion-reaction character of the flow. On top of this, plasma state, divertor target geometry as well as the magnetic configuration are coupled in a complicated way. However, in current edge transport models they are treated independently from each other by relying on precomputed and then fixed magnetic field configurations.

A first step towards a more efficient design methodology was the introduction of an automated procedure for design of the divertor target geometry by shape optimization [4, 5]. In these papers, Dekeyser et al. illustrated the approach by applying it to a divertor shape for a reduced plasma edge transport model and a particular cost functional. In addition to the divertor shape, also the magnetic field strongly influences the exhaust processes, as it governs plasma flow direction as well as plasma-wetted area by flux expansion. However, besides the removal of heat and helium ashes, the magnetic field should be designed to ensure good and stable confinement as well. In this paper an automated procedure is therefore proposed to improve the heat handling capacity of the divertor by altering the magnetic divertor configuration. In order to achieve this goal, a self-consistently coupled procedure is developed.

The first step comprises analyzing sensitivities of the heat exhaust to changes in the magnetic field. In this step modelling choices are made and simulation procedures are integrated into a single sensitivity code system. To tackle the complex interactions of the magnetic field with the confined plasma, a perturbation approach is used. Given the magnetic field resulting from this approach, the target heat load is analysed using a slightly simplified plasma transport model. Both the magnetic and the plasma edge model will be presented in the next section, along with an overview of some essential grid generator adjustments needed to join both models in the integrated approach. Subsequently, the optimization framework for automated magnetic field design is set up in section 3. These automated methods are first formulated in a general fashion as they can analogously be applied to other models. Next, they are elaborated for the specific problem under consideration. Finally, the entire approach is illustrated with a sample

case with typical Joint European Torus (JET) [6] parameters in section 4.

2. Modelling for magnetic field and plasma edge simulations

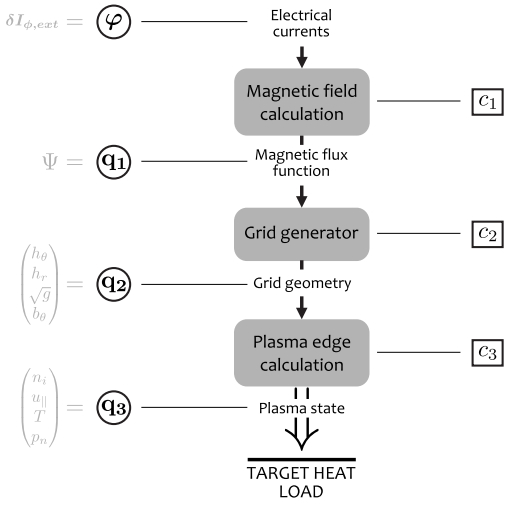

Figure 1. The building blocks necessary to do a forward simulation.

An integrated approach to sensitivity calculation is a critical step to enable analyzing and optimizing divertor concepts. All essential code parts that need to be integrated into one sensitivity code are illustrated in figure 1. A range of models with different levels of sophistication could be selected to simulate the magnetic field and plasma edge flows. In order to demonstrate the optimization techniques in the next section, we introduce a reduced plasma edge transport model compared to B2-Eirene in this section, which meets the requirement of low computational costs but retains most principal dependencies. At a later stage in the design process, one can replace both the magnetic field and the plasma edge transport model with state-of-the-art simulation techniques and do a few optimization cycles using these very same or slightly adjusted design methods on the more extended models. By doing so, a more accurate optimized design might be achieved, still bearing in mind that model deficiencies might influence the optimal solution. In the first part of this section a very fast and simple model is presented to account for small changes to a magnetic equilibrium. In the second part of this section, a reduced plasma edge model is presented to evaluate target heat loads. Finally, a grid generator is responsible for translating magnetic field information into geometric and discretized magnetic information (e.g. the magnetic field pitch in our present model) for the plasma grid. Some remarks on how to adjust a grid generator to the specific demands in this coupled procedure are summarized in the third part of this section.

2.1. Magnetic field modelling

In order to obtain the poloidal magnetic flux Ψ, hereafter referred to as the magnetic flux, for a 2D (axisymmetric) toroidal plasma (tokamak) configuration, and hence the proper curvilinear coordinates for the plasma flow problem, the Grad-Shafranov equation for an ideal static magnetohydrodynamic (MHD) equilibrium is solved in the main plasma [7],

$$\Delta^* \Psi \left(R, Z\right) = -FF' - \mu_0 R^2 p', \tag{1}$$

with $p(\Psi)$ the pressure flux function, $F(\Psi) = RB_\phi$ a flux function associated to the toroidal magnetic field B_ϕ, (R, Z) a coordinate system corresponding to major radius and height, and where the prime denotes a derivative with respect to the magnetic flux Ψ. This equation describes a balance of pressure gradients with Lorentz forces. Everywhere in and around the reactor, the magnetic flux $\Psi\left(R, Z\right)$ is related to the toroidal current density J_ϕ (via Ampère's law) by:

$$\Delta^* \Psi = -\mu_0 R J_\phi, \tag{2}$$

with μ_0 the magnetic permeability of vacuum (not considering dia-, para- or ferromagnetic structures), J_ϕ the toroidal current density (internal and external currents) and the elliptic operator Δ^* being defined as:

$$\Delta^* \Psi = R \frac{\partial}{\partial R} \left(\frac{1}{R} \frac{\partial \Psi}{\partial R} \right) + \frac{\partial^2 \Psi}{\partial Z^2}. \tag{3}$$

We start by taking an unperturbed magnetic equilibrium Ψ_0 of a divertor configuration and a corresponding current density distribution $J_{\phi,0}$, which fulfill (1) and (2). The effect of additional small external current densities $\delta J_{\phi,ext}$ is described as a perturbation $\delta\Psi$ to Ψ_0, using the linear relation:

$$\Delta^* \Psi = \Delta^* \left(\Psi_0 + \delta\Psi\right) = \Delta^* \Psi_0 + \Delta^* \delta\Psi = -\mu_0 R \left(J_{\phi,0} + \delta J_{\phi,int} + \delta J_{\phi,ext}\right), \tag{4}$$

which can be reduced to

$$\Delta^* \delta\Psi = -\mu_0 R \left(\underbrace{\delta J_{\phi,int}}_{\approx 0} + \delta J_{\phi,ext} \right), \tag{5}$$

since $(\Psi_0,\ J_{\phi,0})$ fulfill (2) by definition. Here, the current densities $\delta J_{\phi,int}$ and $\delta J_{\phi,ext}$ are separated to differentiate between the induced plasma currents and the imposed additional external conductor currents required to obtain the magnetic field change $\delta\Psi$. The changes of the internal currents $\delta J_{\phi,int}$ are the hardest to calculate, as they are indirectly dependent on the external currents $\delta J_{\phi,ext}$ through induced shifts in the flux functions p and F. The so called "vacuum approximation" (VA) consists in neglecting the correction term $\delta J_{\phi,int}$ as well as the presence of any dia-, para- or ferromagnetic solid materials. The approach is illustrated in figure 2.

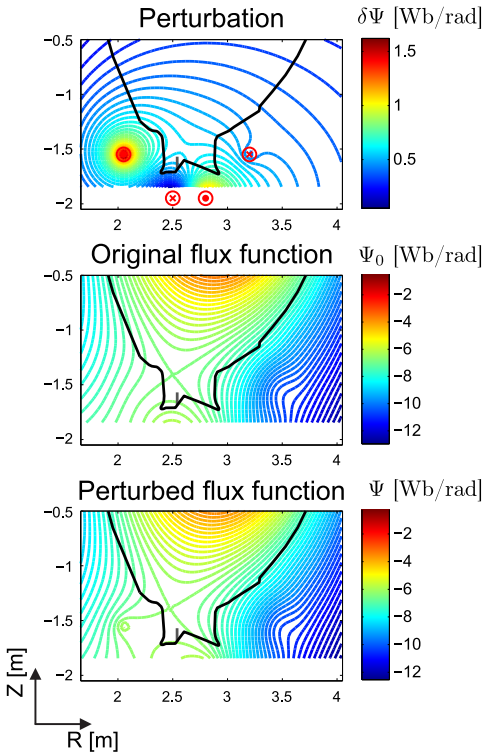

Figure 2. A perturbed magnetic flux Ψ (bottom) is evaluated by adding a calculated perturbation $\delta\Psi$ (top) onto an initial equilibrium Ψ_0(middle). Notice the local changes in the divertor region of the perturbed magnetic flux compared to the reference magnetic flux.

Because of this assumption, force balance, and hence Equation (1), will in general no longer strictly apply if $\delta\Psi \neq 0$. A first order estimate of the error can be found from a linearization of the Grad-Shafranov equation, which provides a condition for $\delta J_{\phi,int}$ from the static force equilibrium inside the plasma:

$$\Delta^*\Psi_0 + \Delta^*\delta\Psi = -(F_0 + F_0'\delta\Psi)(F_0' + F_0''\delta\Psi) - \mu_0 R^2(p_0' + p_0''\delta\Psi) \tag{6}$$

$$= -\mu_0 R\left(J_{\phi,0} + \delta J_{\phi,int}\right), \tag{7}$$

where the '0'-subscripts at the flux functions p and F denote an evaluation at the reference magnetic flux Ψ_0. Remark that the external current changes $\delta J_{\phi,ext}$ are not present in the Grad-Shafranov equation as they only appear as boundary conditions for the solution of the plasma. After subtraction of the unperturbed Grad-Shafranov equation, with reference magnetic flux Ψ_0, and by keeping only first order terms, a description of the error made on the internal plasma currents can be found:

$$\delta J_{\phi,int} = \frac{1}{\mu_0 R}(F_0 F_0'' + F_0'^2)\delta\Psi + R p_0''\delta\Psi. \tag{8}$$

Although technically the $\delta\Psi$ from this equation depends again on the resulting $\delta J_{\phi,int}$, a qualitative conclusion can be drawn from this result. As Grad-Shafranov solvers typically assume that the flux functions F and p are constant in the edge region, the

VA becomes more accurate when the changes to the magnetic flux $\delta\Psi$ only significantly affect the divertor and plasma edge region. In this case all terms on the right hand side of (8) are approximately zero everywhere, and hence also the response current $\delta J_{\phi,int}$. For example, this condition is realized if the divertor shaping coils are close to each other, have opposite current directions and similar magnitude.

To speed up magnetic field calculations even further, the additivity of linearized perturbations $\delta\Psi$ of the magnetic flux can be used to calculate the magnetic field contribution for each conductor separately. Assuming an infinitesimally thin toroidal conductor at (r', z') and making use of the VA, one can derive an explicit expression for the magnetic flux perturbation from additional external currents [8]:

$$\delta\Psi\left(R,Z,r',z'\right)=\frac{-\mu_0 R\,\delta I_{\phi,ext}}{k\pi}\sqrt{\frac{r'}{R}}\left[\left(1-\frac{k^2}{2}\right)K(k)-E(k)\right], \tag{9}$$

where

$$k^2=\frac{4Rr'}{\left(R+r'\right)^2+\left(Z-z'\right)^2}, \tag{10}$$

$\delta I_{\phi,ext}$ is the additional external conductor current and K and E are complete elliptical integrals of the first and second kind. These are respectively given by

$$K(k)=\int_0^{\frac{\pi}{2}}\frac{d\theta}{\sqrt{1-k^2\sin^2\theta}}, \tag{11}$$

$$E(k)=\int_0^{\frac{\pi}{2}}\sqrt{1-k^2\sin^2\theta}\;d\theta. \tag{12}$$

When n_c conductors are present, the total perturbation can be obtained using additivity of (9). Using the approach presented above, small changes to the magnetic field can be computed very fast by evaluation of the elliptic integrals (11) and (12) at positions (R, Z) once and substitution in (9). Afterwards, the fields resulting from the individual conductors only need to be rescaled to find $\delta\Psi$ for other $\delta I_{\phi,ext,i}$. In contrast to the Grad-Shafranov equation, a space discretization method is not needed here for the solution of $\delta\Psi$.

An explicit formulation to compute the magnetic flux Ψ is now at hand. However, as will become clear later, we formulate it now in implicit form to define the magnetic state equations $c_1\left(\boldsymbol{\varphi},\boldsymbol{q_1}\right)=0$, with

$$c_1=\sum_i^{n_c}\frac{-\mu_0 R\,\delta I_{\phi,ext,i}}{k_i\pi}\sqrt{\frac{r_i'}{R}}\left[\left(1-\frac{k_i^2}{2}\right)K(k_i)-E(k_i)\right]+\Psi_0-\Psi. \tag{13}$$

The magnetic flux Ψ will further be referred to as the magnetic state $\boldsymbol{q_1}$ and the shaping conductor currents $\delta I_{\phi,ext,i}$ can be combined into the vector $\boldsymbol{\varphi}$, representing the control or design variables (see section 3).

2.2. Plasma edge modelling

The same edge plasma transport model as in [9] is used to model a single species plasma with ion mass m and charge state Z_i in a poloidal cross section of a toroidally symmetric tokamak. Particle and momentum conservation equations are solved for the ion density n_i and ion parallel velocity $u_\parallel$. The neutral flow is modelled using a pressure diffusion equation, which is solved for the neutral pressure p_n. An internal energy equation is solved for a combined ion-electron-neutral temperature T. To simplify notation we introduce the vector of plasma state variables $\boldsymbol{q_3} = (n_i, u_\parallel, T, p_n)^T$. The plasma transport equations can be written succinctly as $c_3(\boldsymbol{q_2}, \boldsymbol{q_3}) = 0$, with

$$\begin{aligned} c_3 =& \frac{1}{\sqrt{g}}\frac{\partial}{\partial\theta}\left(\frac{\sqrt{g}}{h_\theta}C^\theta - \frac{\sqrt{g}}{h_\theta^2}D^\theta\frac{\partial \boldsymbol{q_3}}{\partial\theta}\right) \\ &+ \frac{1}{\sqrt{g}}\frac{\partial}{\partial r}\left(\frac{\sqrt{g}}{h_r}C^r - \frac{\sqrt{g}}{h_r^2}D^r\frac{\partial \boldsymbol{q_3}}{\partial r}\right) - S, \end{aligned} \tag{14}$$

$C^\theta = (n_i u_\theta, m n_i u_\theta u_\parallel, \frac{5}{2}(1+Z_i) n_i u_\theta T, 0)^T$ and $C^r = 0$ the poloidal and radial convective flux, $u_\theta = b_\theta u_\parallel$ the ion poloidal velocity, and $\boldsymbol{q_2}$ a vector containing magnetic geometry information from the grid generator (described in section 2.3). $D^\theta = \mathrm{diag}(0, \eta^\theta, \kappa^\theta, D_{p_n})$ and

$$D^r = \begin{pmatrix} D_i^r & 0 & 0 & 0 \\ m D_i^r u_\parallel & \eta^r & 0 & 0 \\ \frac{5}{2}(1+Z_i) D_i^r T & 0 & \kappa^r & 0 \\ 0 & 0 & 0 & D_{p_n} \end{pmatrix}$$

are matrices containing respectively the poloidal and radial diffusive coefficients. The above equations are augmented with the equations for plasma and for neutral pressure, respectively $p = (1+Z_i) n_i T$ and $p_n = n_n T$. The sources $S(\boldsymbol{q_2}, \boldsymbol{q_3})$ are defined as

$$S = \begin{pmatrix} n_e n_n K_i - n_i n_e K_r \\ -\frac{b_\theta}{h_\theta}\frac{\partial p}{\partial\theta} - m n_i n_e K_r u_\parallel - m n_i n_n K_{cx} u_\parallel \\ -E_i n_e n_n K_i - c_z n_i n_e L_z \\ n_i n_e K_r - n_e n_n K_i \end{pmatrix},$$

with E_i the energy lost by the plasma at ionization and $n_e = Z_i n_i$ the electron density. The contribution of the neutral velocity $u_{n\parallel}$ is left out in the ion momentum source as the neutral velocities resulting from this simple pressure-diffusion model tend to be unrealistically high. The impurity radiation is based on a prescribed, spatially constant impurity fraction c_z. Rate coefficients K_i, K_r and K_{cx} for electron impact ionization, radiative recombination and charge-exchange, respectively, as well as the radiative loss function L_z of Carbon are approximated using the same analytical expressions as given in [4]. The isotropic neutral pressure diffusion coefficient D_{p_n} is determined by a reformulation of the neutral momentum equation, where the latter is reduced to a balance between pressure gradient force and momentum source terms. Thus, the

coefficient is given by

$$D_{p_n} = \frac{1}{m\left(n_i K_{\mathrm{cx}} + n_e K_{\mathrm{i}}\right)}. \tag{15}$$

Similar expressions can be found in a.o. [10]. Finally, the expression $\kappa_n = \chi_n p_n D_{p_n}$ is used for the neutral conductivity, while transverse plasma conductivity and ion viscosity are respectively given by $\kappa_r = nD_\kappa$ and $\eta_r = mn_i D_i^r$. It should be noted that alternative formulations of the neutral fluid model and its interaction with the edge plasma are also used, see e.g. [5]. Ultimately more accurate neutral models as simulated with Monte Carlo codes (e.g. EIRENE) are desirable. Similarly, the introduction of a multispecies plasma edge model might improve the accuracy of the radiation calculation. We deliberately keep the plasma edge model as simple as possible while including main features to provide first results and the basic principles of our new design approach. Improved modelling issues are planned to be addressed in future work.

2.3. Plasma edge grid generation

High quality computational grids for solving the plasma edge transport equations are needed, in order to obtain accurate sensitivities of plasma edge quantities with respect to the magnetic field configuration. Due to the highly anisotropic transport in the plasma edge, the plasma edge equations are preferentially solved on quadrilateral grids aligned with the magnetic field in order to avoid numerical diffusion. Two sides of these cells then coincide with surfaces of constant Ψ, while the other two are made as orthogonal as possible. The consequence is that every change in magnetic field induces a corresponding change in plasma edge grid. Therefore, the grid generator $c_2\left(\boldsymbol{q_1}, \boldsymbol{q_2}\right)$ is a substantial part of the coupled simulation chain and must generate grids for the numerical solution of $c_3\left(\boldsymbol{q_2}, \boldsymbol{q_3}\right) = 0$ in a completely automated fashion.

In order to create high quality grids, all spatial gradients should be sufficiently resolved. Therefore, it is necessary to have a fine radial discretization towards the separatrix. Conversely, the poloidal resolution of the 2D grid can be rather crude near the midplane, which results in cells with a high aspect ratio. Further, the divertor region requires a strong poloidal grid refinement and a continuous adjustment of the nearly orthogonal grid at the midplane towards a grid aligned with the target shape. Here, no iterative procedure is used to enhance grid orthogonality in this region in contrast to most current plasma edge grid generators, such as CARRE [11]. Non-orthogonality in plasma edge computation will now be tackled with an appropriately enhanced discretization scheme. The absence of this iterative procedure improves the predictability of the grid generation process, which facilitates the robust grid generation under different magnetic field inputs.

The automation of the grid generation needs some additional care. A first issue arises when detecting X- and O-point of the magnetic configuration as this often requires additional, case specific, input. Indeed, X- and O-point can be detected by calculating the locations where $\nabla\Psi = 0$. However, in general secondary X- and O-points may be

present. Hence, a criterion that the new primary X- and O-point should be nearby their respective original locations is added. Secondly, the outer radial boundaries of the grids should be selected in an appropriate way: the influence of the boundary conditions imposed here should be as small as possible as they are typically very crude (constant decay length boundary conditions for ion density and temperature and a recycling condition for neutrals). Therefore, the simulated region is chosen to extend to the vessel wall as far as possible. In addition, the approximations for the objective functional, as will be explained in section 3.1, will benefit from these distant radial boundaries. However, the choice of these grid boundaries is limited by the basic assumption made by most plasma edge solvers that the grid boundary should be a magnetic flux surface that is fully contained, from target to target, in the vessel. For all these reasons we dynamically select the outermost magnetic flux surface that does not cross any solid material in between the divertor targets. In the private flux region, such a boundary can not always be found. Therefore, it is chosen to add a fictitious 'limiter' that limits the radial extent of the simulated plasma in the private flux area (grey solid line in figure 3). Alternatively, a discretization scheme reaching all the way up to the reactor wall, as elaborated in [12], would be a natural way to approach this grid boundary problem.

Finally, in order to verify robust behaviour of the grid generator, a test procedure with random inputs was implemented. This procedure generates a series of possible combinations for the control currents that obey both the box constraints on the current magnitudes and the core shape constraints. Both will be discussed in section 3.2. Using (13), the magnetic flux is computed and a grid generation is attempted. Grid generator errors and twisted cells are automatically detected and listed. Based on the results of these random input tests, implementations were generalized, and grid as well as constraint parameters were tuned to have the best overall grid performance. In this way, the chances that the simulations do not converge during the optimization cycle are minimized.

3. General set-up for automated design using optimization methods

In order to achieve automated design, it is necessary to reformulate the design problem in an optimization setting. This is a crucial exercise, which involves defining how designs should be compared, to what extent parameters can be controlled and which designs are desirable or impossible. In this paper, the design focus will be on spreading the target heat flux as homogeneously as possible, by means of magnetic field changes only. However, the optimization framework is very well suited for finding compromises between several design goals and constraints, such as simultaneously improving the pumping capability of the configuration as well. The variables $\boldsymbol{\varphi}$ used to design the magnetic field in the present work are the electrical currents $\delta I_{\phi,ext,i}$ in spatially fixed

external toroidal coils. The optimization problem can then be written formally as

$$\begin{aligned} \min_{\boldsymbol{\varphi}\in\Phi_{ad},\boldsymbol{q_1},\boldsymbol{q_2},\boldsymbol{q_3}} \quad & \mathcal{I}\left(\boldsymbol{\varphi},\boldsymbol{q_1},\boldsymbol{q_2},\boldsymbol{q_3}\right) \\ s.t. \quad & c_1(\boldsymbol{\varphi},\boldsymbol{q_1})=0, \\ & c_2(\boldsymbol{q_1},\boldsymbol{q_2})=0, \\ & c_3(\boldsymbol{q_2},\boldsymbol{q_3})=0, \\ & h_i(\boldsymbol{\varphi},\boldsymbol{q_1})\leq 0, i=1\ldots n, \end{aligned} \tag{16}$$

where $\mathcal{I}$ is the objective functional evaluating the heat spreading, $h_i \leq 0$ the design constraints that might be in place, and Φ_{ad} a set of admissible values for the control variables $\boldsymbol{\varphi}$, which takes direct constraints into account. c_1, c_2 and c_3 represent respectively the magnetic field evaluation with the control currents as an input, the grid generator that converts the magnetic flux into discretized geometric magnetic field information, and the plasma edge simulation that uses the latter to simulate the plasma state (see figure 1). In our optimization formulation, we can, in principle, use the equations $c_1 = 0$, $c_2 = 0$, and $c_3 = 0$ to eliminate the state variables $\boldsymbol{q_1}$, $\boldsymbol{q_2}$ and $\boldsymbol{q_3}$ from the optimization problem. The so-called *reduced* optimization problem is then given by

$$\begin{aligned} \min_{\boldsymbol{\varphi}\in\Phi_{ad}} \quad & \widehat{\mathcal{I}}\left(\boldsymbol{\varphi}\right)=\mathcal{I}\left(\boldsymbol{\varphi},\boldsymbol{q_1}\left(\boldsymbol{\varphi}\right),\boldsymbol{q_2}\left(\boldsymbol{q_1}\left(\boldsymbol{\varphi}\right)\right),\boldsymbol{q_3}\left(\boldsymbol{q_2}\left(\boldsymbol{q_1}\left(\boldsymbol{\varphi}\right)\right)\right)\right) \\ s.t. \quad & \widehat{h_i}(\boldsymbol{\varphi})=h_i(\boldsymbol{\varphi},\boldsymbol{q_1}\left(\boldsymbol{\varphi}\right))\leq 0, i=1\ldots n, \end{aligned} \tag{17}$$

with $\widehat{\mathcal{I}}\left(\boldsymbol{\varphi}\right)$ the reduced cost functional and $\widehat{h_i}(\boldsymbol{\varphi})$ the reduced constraints, which can be combined into a constraint vector $\widehat{\boldsymbol{h}}(\boldsymbol{\varphi})$. The resulting optimization problem is then reduced in the sense that the simulation chain is implicitly performed to obtain the cost functional in such a way that these constraints and their state variables $\boldsymbol{q_1}$, $\boldsymbol{q_2}$ and $\boldsymbol{q_3}$ do not have to be accounted for explicitly in our optimization framework. This is a fundamentally different way of implementing the optimization problem. In the reduced framework, plasma edge and magnetic field problems are treated as 'black box solvers' which compute state variables for given control variables. The optimization code is only responsible for finding the optimal value of the control variables, and can be built as an additional optimization layer around the existing simulation codes. In problem (16), on the other hand, all state variables are treated as control variables in the optimization problem as well, which are subject to the state constraints. The optimization problem thus has much higher dimensionality, but very efficient tailored algorithms may be developed which exploit the specific problem structure, e.g. one-shot methods [13, 14]. The magnetic and plasma edge models were elaborated in the previous section. All other components of the optimization problem will be considered in more detail in the remainder of this section. In Appendix A, the solution method for this optimization problem is presented.

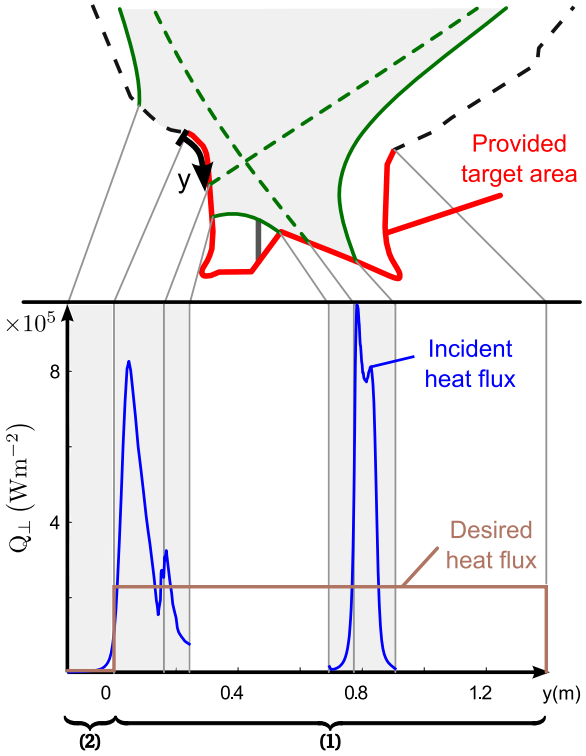

Figure 3. Computation of the objective functional. Outer grid boundaries (solid green lines), gridded area (grey area), and predefined target area (red) are illustrated in a close-up of the divertor region (top). Difference between the desired (brown) and initial (not optimized, blue) heat flux along the projected target area coordinate 'y' (bottom). (1) and (2) correspond to the surface over which is integrated for terms (1) and (2) of Equation (19), respectively

3.1. A suitable objective functional formulation

Following Dekeyser [5], the objective functional representing the level of heat spreading can be expressed by

$$\mathcal{I}_0\left(\boldsymbol{\varphi}, \boldsymbol{q_1}, \boldsymbol{q_2}, \boldsymbol{q_3}\right) = \frac{1}{2}\int_{S_t}\left(Q_\perp - Q_{d,t}\right)^2 d\boldsymbol{\sigma}, \tag{18}$$

where S_t denotes the target area, $Q_\perp$ the heat flux density perpendicular to the target surface and $Q_{d,t}$ a desirable spatially constant heat flux profile. $\mathcal{I}_0\left(\boldsymbol{\varphi}, \boldsymbol{q_1}, \boldsymbol{q_2}, \boldsymbol{q_3}\right)$ is minimal when the whole target area is uniformly loaded. In this case the best design relative to this particular choice of cost functional and plasma model is achieved. The computation of the objective functional is illustrated in figure 3. The target area S_t is a fixed predefined part of the vessel chosen by the designer to serve this purpose.

A practical problem is that not necessarily all heat load values for the target area are available, as parts of the area may not be covered by the computational grid. It can be assumed however that in these regions, either far into the scrape-off layer (SOL)

or private flux (PF) zone, heat fluxes are orders of magnitude lower than those near the separatrix. Moreover, as the grid extends to the flux surface that just touches solid material, the radial decay of heat flux towards PF zone or to the far SOL from this radial point on will be even steeper, due to shorter connection length further out. Therefore, we choose to neglect parallel target heat fluxes outside the numerical grid. It should be noted that these neglected zero heat fluxes do have a contribution to the cost functional, as the integration of (18) is over the entire predefined target area, including the parts outside the numerical grid. This contribution stimulates better use of this part of the target area, e.g. by flux expansion. For a more precise treatment a discretization scheme reaching all the way up to the reactor wall, as elaborated in [12], should be considered.

As the first wall is not included into the objective functional (18), care has to be taken that the optimization procedure is not misled by a deflection of heat fluxes towards the first wall components to realize a decrease in cost functional. Therefore, a penalty term is added to the objective functional (term (2) in Equation (19) below). By setting the desired heat flux to the first wall $Q_{d,p}$ equal to zero, this term becomes zero when there is no parallel heat flux towards the first wall. To ensure convergence of the optimization problem, a regularization term is added (term (3) in Equation (19) below). Notice that in this case, the regularization term also has economical relevance, since it avoids configurations with large additional shaping currents.

The total objective functional then becomes

$$\begin{aligned}\mathcal{I}\left(\boldsymbol{\varphi}, \boldsymbol{q_1}, \boldsymbol{q_2}, \boldsymbol{q_3}\right) =& \lambda_Q \left(\underbrace{\mathcal{I}_0}_{(1)} + \underbrace{\frac{1}{2}\int_{S_P} \left[\lambda_P \left(Q_\perp - Q_{d,p}\right)\right]^2 d\sigma}_{(2)} \right) \\ &+ \underbrace{\frac{1}{2}\lambda_\varphi \sum_i \boldsymbol{\varphi}_i^2}_{(3)},\end{aligned} \tag{19}$$

where S_P is the area outside the predefined target area and λ_P, λ_Q, and λ_φ are weighting variables for the related terms. Additionally, λ_Q and λ_φ contain characteristic quantities for heat flux and current, respectively, to make the cost functional dimensionless and about unity.

3.2. Introducing a core shape constraint

Given the objective functional of equation (19), it might be desirable to additionally define constraints for the optimization problem. This might firstly be done from a modelling perspective. Indeed, depending on the algorithms used for the three simulation blocks, the models might not be generally applicable for any $\boldsymbol{\varphi}$. Generalizing these blocks is very time-consuming and is often conflicting with our demand for acceptably fast simulations and optimization. A trade-off therefore arises. Either the models are improved for automated usage, or alternatively additional constraints are

introduced to define practical working limits. For example, a box constraint on the current can be applied to limit the errors made by the perturbation approach to magnetic field calculations presented in section 2. This means that an upper and lower limit for all currents are set:

$$\varphi_i \in [\varphi_{i,\min}, \varphi_{i,\max}] \,. \tag{20}$$

Likewise, such constraints can be tuned to achieve robust grid generation in the feasible set (set of allowed current combinations), e.g. avoiding multiple X-points. It should be noted that the latter constraint is at present mainly introduced to avoid additional complexity in plasma edge simulations.

A second reason to introduce constraints might be to incorporate design requirements not accounted for by the objective functional. For example, even for small

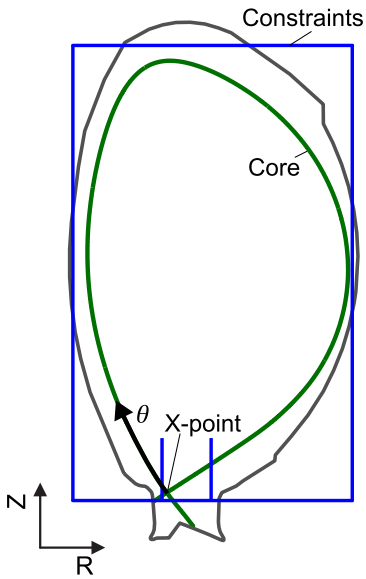

Figure 4. The constraints on the separatrix movement.

magnetic field changes as will be considered in this work, the core might outgrow the vessel, causing a loss of confinement. This is of course undesirable from both a design as well as a robust simulation perspective. The resulting limiter configuration would not meet design requirements as the provision of sufficient neutral pumping possibilities or the guarantee of sufficient core purity. Therefore additional (indirect) constraints on $\boldsymbol{\varphi}$ are put in place to prevent this phenomenon. A practical solution to guarantee confinement is constraining the plasma core spatially within a box, as illustrated in figure 4. Numerically, the choice of constraints in figure 4 can be translated into inequality

constraints:

$$\begin{aligned} h_1 &= \max_{\theta\in\theta_{\text{core}}} \left(R_{\text{core}}(\theta)\right) - R_{\max} \leq 0, \\ h_2 &= \max_{\theta\in\theta_{\text{core}}} \left(Z_{\text{core}}(\theta)\right) - Z_{\max} \leq 0, \\ h_3 &= R_{\min} - \min_{\theta\in\theta_{\text{core}}} \left(R_{\text{core}}(\theta)\right) \leq 0, \\ h_4 &= Z_{\min,\text{X}} - Z_{\text{X}} \leq 0, \\ h_5 &= R_{\min,\text{X}} - R_{\text{X}} \leq 0 \qquad \text{and} \\ h_6 &= R_{\text{X}} - R_{\max,\text{X}} \leq 0, \end{aligned} \tag{21}$$

with θ the coordinate along the last closed flux surface, $R_{core}\left(\theta\right)$ and $Z_{core}\left(\theta\right)$ the parametrization of the core boundary, subscript X referring to the location of the X-point and R_{min}, R_{max}, Z_{max}, $Z_{\min,\text{X}}$, $R_{\min,\text{X}}$ and $R_{\max,\text{X}}$ preset values for the constraint box. Convexity of the core shape is assumed so that there cannot be multiple outer core points and the gradient of these inequality constraints thus always exists.

3.3. Projection onto the separatrix box

As inequality constraints are in general only obeyed after convergence of the optimization problem, intermediate states of the optimization problem might demand evaluating objective functional values for which these constraints are not obeyed. This means that the core might be well outside the described box. Unfortunately grid generation and therefore plasma calculations and objective functional evaluations would be impossible in this case. The optimization procedure thus has to obey these constraints at any time. This is achieved by projecting the currents to the closest point in the admissible design space (i.e. the point with the smallest change in currents), which does satisfy all constraints. In optimization theory, this method is generally referred to as the "gradient projection method". As the separatrix box constraint is strongly nonlinear, the projection $\boldsymbol{\varphi} = \mathcal{P}\left(\bar{\boldsymbol{\varphi}}\right)$ of a point $\bar{\boldsymbol{\varphi}}$ onto a point $\boldsymbol{\varphi}$ that obeys all constraints is an optimization problem by itself [15] and is given by

$$\mathcal{P}\left(\bar{\boldsymbol{\varphi}}\right) = \arg\min_{\boldsymbol{\varphi}\in\Phi_{ad}} \left|\left|\boldsymbol{\varphi} - \bar{\boldsymbol{\varphi}}\right|\right|^2 s.t.\ \widehat{\boldsymbol{h}}(\boldsymbol{\varphi}) \leq 0, \tag{22}$$

with $||\cdot||$ the Euclidean norm, and "arg min" the argument $\boldsymbol{\varphi}$ for which the function is minimal.

As this optimization problem can be as complex as the initial optimization problem, gradient projection methods are in general only used in combination with linear control constraints. However, in our case, the inequality constraints only depend on magnetic field variables and the magnetic field computation is many times faster than the plasma edge simulation. Therefore, the gradient projection method turns out to be appropriate here.

4. Automated design procedure applied to a JET configuration

4.1. Test case specification

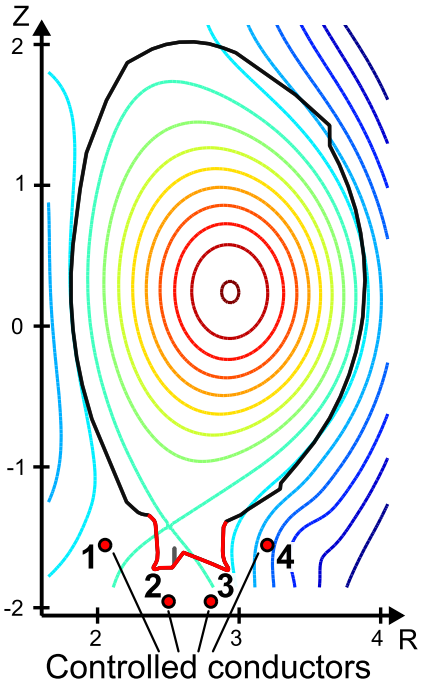

Figure 5. The set-up for magnetic field design. Four new conductors (numbered) are placed near the predefined target area (red). The contour lines are magnetic flux surfaces.

In this section the novel automated design method is, in a first feasibility study, applied for a JET reference configuration obtained from earlier numerical edge transport studies [16]. Model parameters (detailed below) are chosen to keep the edge transport model as simple as possible (low recycling conditions) to focus the attention on the capability of the magnetic optimization aspects in this first illustrative application. The initial magnetic field is an EFIT reconstruction of an experimental L-mode JET shot 80966 named HT3L from the c28b JET campaign (2011). It is characterized by a horizontal outer target, a high triangularity ($\delta = 0.38$) and $I_p/B_T = 0.8$ MA T^{-1}. The magnetic configuration is displayed in figure 5. The electric currents that will be optimized are those going through four fictitious conductors that are added near the divertor targets to have an as large as possible local impact on the magnetic field. The number of conductors is set to four to keep the computational costs for gradient computations limited. These conductors, as well as the target area used in the cost functional formulation (19), are illustrated in the same figure. Apart from the box constraints on the design currents, a linear constraint

$$\varphi_{\text{minsum}} \leq \sum_{i=1}^{n_{\boldsymbol{\varphi}}} \varphi_i \leq \varphi_{\text{maxsum}} \tag{23}$$

is introduced to limit the change to the more distant core magnetic field and the according loss of grid quality and magnetic model validity. Additionally, the separatrix constraints introduced in section 3.2, which depend nonlinearly on the control currents, have to be fulfilled (see table 1).

	position [m]	min. $\boldsymbol{\varphi}$ [kA]	max. $\boldsymbol{\varphi}$ [kA]
$\boldsymbol{\varphi}_1$	$(2.05, -1.55)$	-61	61
$\boldsymbol{\varphi}_2$	$(2.50, -1.95)$	-61	61
$\boldsymbol{\varphi}_3$	$(2.80, -1.95)$	-61	61
$\boldsymbol{\varphi}_4$	$(3.20, -1.55)$	-61	61
$\sum_{i=1}^{n_{\boldsymbol{\varphi}}} \boldsymbol{\varphi}_i$		-102	102
R_{min}	1.83		
Z_{max}	1.85		
R_{max}	3.85		
$Z_{\text{min,X}}$	-1.44		
$R_{\text{min,X}}$	2.475		
$R_{\text{max,X}}$	2.83		

Table 1. The values of the different parameters that appear in the constraint expressions (20),(21),(23).

The plasma edge simulation is performed on a 240×80 grid. In the parallel direction, plasma transport coefficients are set according to Braginskii [17]. Radial anomalous transport coefficients comprise a radial ion diffusivity $D_i^r = 0.8$ m^{2}s^{-1}, a transverse ion viscosity coefficient $D_\eta = 0.8$ m^{2}s^{-1}, a radial plasma conductivity coefficient $D_\kappa = D_{\kappa_i} + D_{\kappa_e} = 2$ m^{2}s^{-1} and a neutral conductivity coefficient $\chi_n = 0.2$.

At the core boundary the input power ($Q_{\text{in}} = 3$ MW) and the core density ($n_{i,c} = 1.3 \cdot 10^{19}$ m^{-3}) are specified. For the neutrals a leakage condition proportional to the product of local neutral density and thermal speed [18] is given, with proportionality constant 0.2. $u_\parallel = 0$ m^{2}s^{-1} is assumed for the momentum equation at this boundary. Typical sheath conditions are imposed at the divertor targets. At the outermost flux surfaces a radial decay length is assumed for plasma density ($\lambda_n = 0.05$ m) and temperature ($\lambda_T = 1$ m). This temperature decay length is large in comparison to models with a separate energy equation for the neutrals to account for the dominant contribution of the latter to heat transport in the far SOL [18]. All ions reaching wall and target domain boundaries are recycled as neutrals. At the private flux the same recycling condition is kept, but additionally neutrals are pumped here. As the area of the last private flux surface is varied during simulations, we keep the effective pumping fixed for an assumed constant boundary temperature. The pumping speed is given in

[m^3/s] by [19]

$$N_p = A\ p_a\ 36.38\sqrt{\frac{T}{m}}, \tag{24}$$

with A the surface over which particles are pumped in the model, p_a the sticking fraction, T the particle temperature [K] and m the particle mass [a.m.u.]. An effective pumping speed $N_p = 7.34\ \mathrm{m^3 s^{-1}}$ at room temperature is maintained in all simulations. The above formula is then used to compute a spatially constant sticking fraction along the private flux boundary. The local pumping flux density is computed using the sticking fraction as proportionality constant in a leakage boundary condition similar to the treatment of the core boundary. Our choice of model parameters results in low recycling divertor conditions, as a nearly constant temperature profile along flux surfaces in the divertor region and a linear relation between target particle flux and upstream density were observed.

4.2. Results

Two magnetic field optimization applications will be discussed in this section. They differ in weightings for the heat flux in term (2) of Equation (19), respectively $\lambda_P = 1$ and $\lambda_P = 10$. The weighting of this wall heating term reflects to what extent one wants to tolerate a higher value for term (1) of Equation (19) to avoid the need for target area expansion. For the case of an existing reactor one could rather try to avoid changing the material configuration at the wall so that the λ_P parameter will be higher. In case of a new design a lower λ_P will explore the opportunity to enlarge the divertor target area. The other objective functional weighting variables are $\lambda_Q = 2.85 \cdot 10^{-12}\ \mathrm{m^2 W^{-2}}$ and $\lambda_\phi = 1 \cdot 10^{-12}\ \mathrm{A^{-2}}$.

4.2.1. Optimization with low wall heating penalty

In figure 6, the change of control variables and cost functional are given for the different optimization stages in case of low wall heating penalty. Starting from zero perturbation currents, negative and positive currents are introduced by the optimization loop to reduce the cost functional value. In figure 6b, the different contributions of equation 19 are presented. Although the total cost functional is decreasing, not every single term in equation 19 is. In this case, one can observe that a compromise is found between decreasing the heat flux to the targets and not increasing too much the wall heating penalty and current penalty.

The dominant reduction in cost functional is achieved by heat spreading over the target surface. To verify this, the simulated target heat flux is displayed in figure 7 at different optimization stages. Indeed, a sharp reduction of the heat peaks is observed at the cost of a tolerable heat flux increase outside the defined target area, as the increased heat peak around $y = 0$ remains well below the other two peaks.

In figure 8, the initial and optimized magnetic fields are shown. It can be observed that the opposing current pairs 1, 2 and 3, 4 (Fig. 6) cause an expansion of the field lines

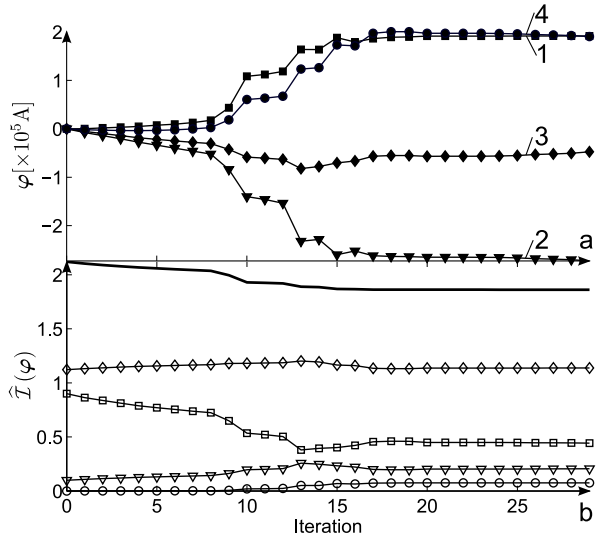

Figure 6. **a)** The change of control current magnitudes (numbers of coils corresponding to fig. 5) and **b)** the change of the different cost functional contributions as a function of the number of optimization iterations performed for $\lambda_P = 1$. —: total cost functional, –◇–and –□–: respectively not simulated and simulated part of term (1) in Equation (19), –▽–: wall penalty (term (2) in Equation (19)), –○–: control (current) penalty (term (3) in Equation (19)).

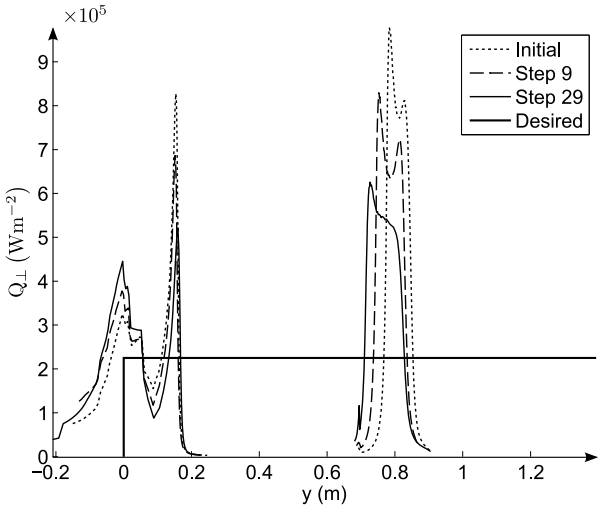

Figure 7. The change in heat loading from initial (···) to optimized (—) magnetic configuration for $\lambda_P = 1$.

at the target area, spreading the heat flux analogously to the X-divertor concept [2]. It should be noted again, however, that this configuration is by no means an optimization in general, in particular not for standard JET operation conditions (high recycling or detached divertor states). The results rather demonstrate that the automated procedure developed here provides plausible trends relative to an underlying physical edge model. Although it is logical to maximize flux expansion in this low recycling test case, an

automated design result for high recycling or even detached conditions might be harder to interpret, and is currently outside the validity range of our still simplified underlying plasma model. Finally, it should be noted that the X-point is constrained to its lower boundary $Z_{\min,X}$ (Table 1).

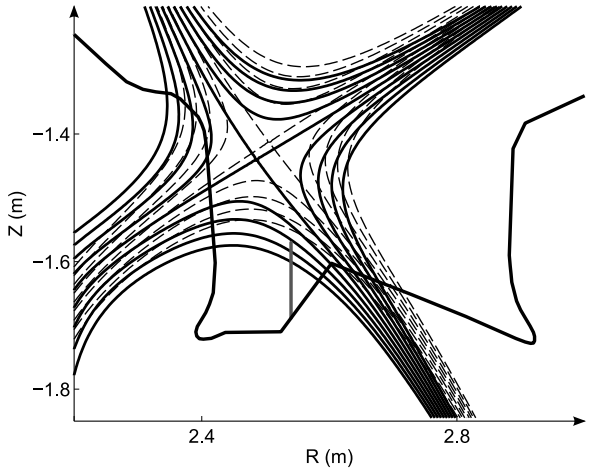

Figure 8. The change in magnetic flux from initial (– –) to the optimized (—) configuration for $\lambda_P = 1$.

4.2.2. Optimization with high wall heating penalty

When increasing λ_P by a factor 10, it is expected that avoiding heat loads outside the predefined target area will become more dominant in the objective functional compared to the other terms. Indeed, according to figure 9b, the main reduction in cost functional is achieved by removing all wall heat load contributions at the inner target in the first optimization step (-▽- curve). It is only afterwards that the target heat term is reduced (-□- curve). In figure 10 the reduction of this wall heating can be verified. In order to achieve this result, the X-point was moved away from the inner target area boundary by the optimization procedure (Figure 11), at the cost of a narrowing of the flux tubes and a corresponding rise in the heat peaks. We note that the only reason that the heat peaks on the target area have been increased is because the original magnetic field did not meet the design requirements as this cost functional implicitly requires a reduced heating outside the target area. When relaxing this design requirement one obviously retrieves again a heat peak reduction, as could be seen for $\lambda_P = 1$.

4.3. Computational cost

In order to give a brief overview

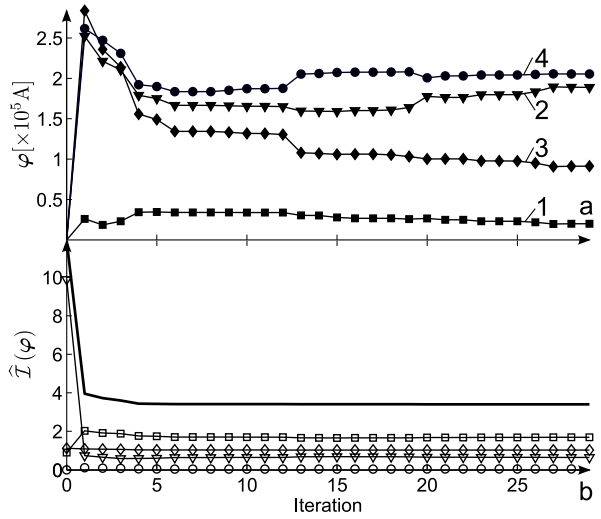

Figure 9. **a)** The change of control current magnitudes (numbers of coils corresponding to fig. 5) and **b)** the change of the different cost functional contributions as a function of the number of optimization iterations performed for $\lambda_P = 10$. —: total cost functional, –◇–and –□–: respectively not simulated and simulated part of term (1) in Equation (19), –▽–: wall penalty (term (2) in Equation (19)), –○–: control (current) penalty (term (3) in Equation (19)).

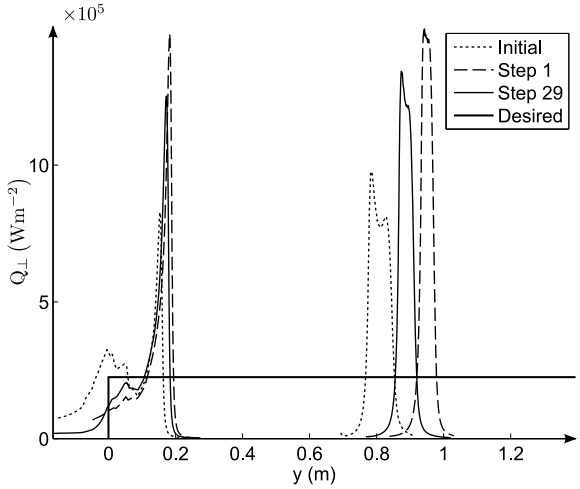

Figure 10. The change in heat loading from initial (···) to optimized (—) magnetic configuration for $\lambda_P = 10$.

5. General conclusions and future perspectives

An optimization based approach for automated magnetic field design of tokomak divertors has been presented. To this end, models for magnetic field and plasma edge were combined with a grid generator into one code that is able to compute sensitivities of plasma edge quantities with respect to the currents that control the magnetic field.

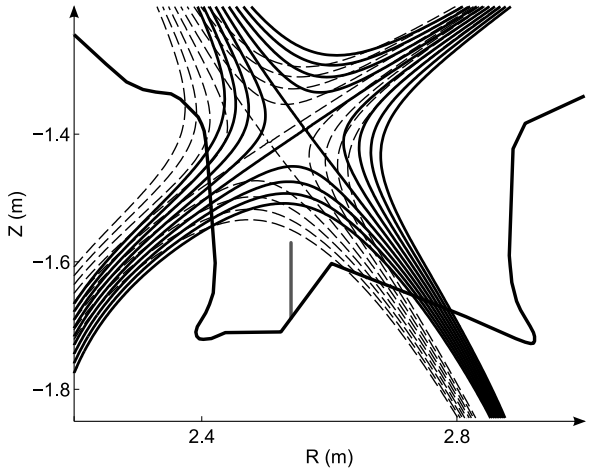

Figure 11. The change in magnetic flux from initial (−−) to the optimized (—) configuration for $\lambda_P = 10$.

A reduced model for magnetic field computations is used, until now only perturbing an initial equilibrium. Special care is taken to ensure design requirements not accounted for in the objective functional, e.g. core purity and neutral pumping, are accounted for by introducing appropriate optimization constraints that prevent the configuration from losing confinement. The optimal design approach has finally been demonstrated on a realistic JET magnetic field as a test case. The results for this reduced plasma edge model seem to indicate that the overall automated optimization loop provides plausible trends, and a significant sensitivity of edge plasma flow solutions with respect to magnetic configuration details. However, the tests are currently still limited by simplifications in the physical edge transport model to arrive at quantitative conclusions for the real operational conditions. However, in order to achieve good results, it is of crucial importance that design requirements are translated correctly into a so-called objective functional. To this end, the influence of different weightings for cost functional terms, representing the relative importance of different design criteria, is investigated for a JET configuration.

Although currently reduced models are used for magnetic field as well as for plasma edge computations, other models can be integrated into the approach too. Plasma edge simulation costs are unfortunately still very high, even for the reduced plasma model. The cost of gradient computation could however greatly be reduced by using the adjoint approach for gradient computation [4]. Using this approach, the time needed for a gradient computation becomes in principle independent of the number of design variables. This would allow for more freedom in the design. Not only could the number of potential perturbation current conductors be increased, but also the positioning of the coils could be optimized. An exploration of adjoint methods for magnetic field design is therefore one of the next steps planned. In addition, future work will explore the incorporation of MHD-stability constraints in the optimization approach.

Acknowledgments

The authors acknowledge support from OPTEC (OPTimization in Engineering Center of excellence KU Leuven), which is funded by the KU Leuven Research Council under grant no PFV/10/002. We acknowledge S. Wiesen for providing the JET equilibrium data.

Appendix A. Solving the optimization problem

In order to solve the optimization problem (16), a Sequential Quadratic Programming (SQP) strategy with damped Broyden-Fletcher-Goldfarb-Shanno (BFGS) Hessian updating is applied [15]. In contrast to other popular optimization methods such as steepest-descent, the SQP approach features a superlinear convergence of the optimization. A schematic overview of the implemented SQP procedure is given in figure A1.

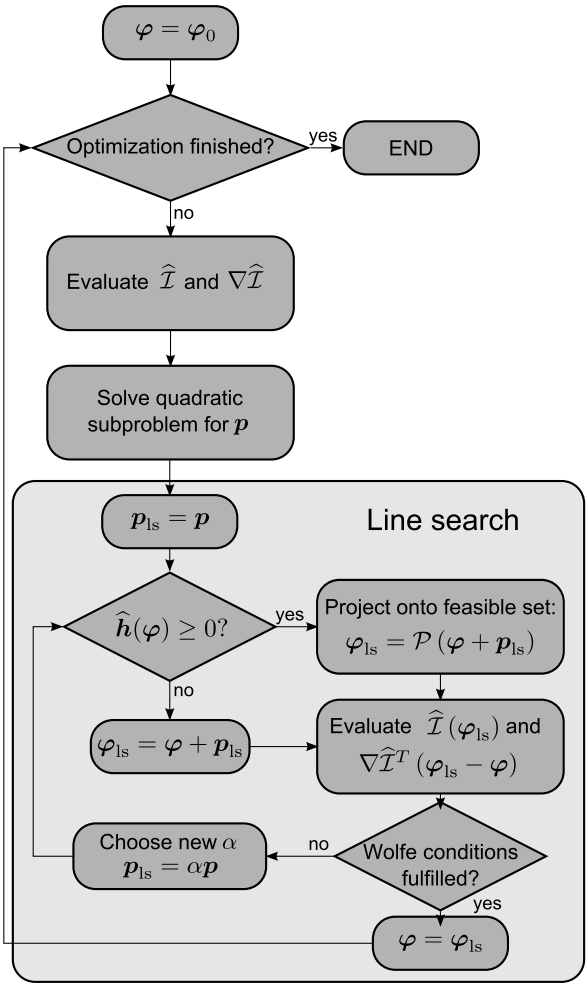

Figure A1. An overview of the implemented SQP optimization algorithm.

The SQP procedure subdivides the original optimization problem in a sequence of

quadratic problems. Hence, the quadratic subproblem in iteration k is given by

$$\begin{aligned} \min_{\boldsymbol{p}\in\Phi_p=\{\boldsymbol{p}|\,\boldsymbol{\varphi_k}+\boldsymbol{p}\in\Phi\}} \quad & \nabla\widehat{\mathcal{I}}\left(\boldsymbol{\varphi_k}\right)^T\boldsymbol{p}+\frac{1}{2}\boldsymbol{p}^T B_k\boldsymbol{p} \\ s.t. \quad & \widehat{\boldsymbol{h}}(\boldsymbol{\varphi}_k)+\nabla\widehat{\boldsymbol{h}}\left(\boldsymbol{\varphi_k}\right)^T\boldsymbol{p}\geq 0, \end{aligned} \tag{A.1}$$

with $\boldsymbol{p}=\boldsymbol{\varphi_{k+1}}-\boldsymbol{\varphi_k}$ the step in control variables that is optimized in each iteration to find a minimum of the local quadratic Taylor expansion of the objective function. The Hessian B_k is not an exact Hessian but rather an approximation by a BFGS algorithm, which uses only gradient information and therefore significantly reduces the computational time needed for one quadratic subproblem evaluation.

The gradients of the objective functional $\nabla\widehat{\mathcal{I}}$ and the contraint function $\nabla\widehat{\boldsymbol{h}}$ with respect to the control variables $\boldsymbol{\varphi}$ are evaluated using finite difference calculations. This means that for a control vector of length $n_{\boldsymbol{\varphi}}$ (e.g. $n_{\boldsymbol{\varphi}}=n_c$, the number of additional shaping coils in our case), $n_{\boldsymbol{\varphi}}+1$ evaluations of these functions are needed. It should be noted that the evaluation of $\nabla\widehat{\mathcal{I}}$ requires many plasma edge simulations and is therefore computationally extremely demanding. On the other hand computing the constraint gradient $\nabla\widehat{\boldsymbol{h}}$ is relatively cheap as it involves magnetic field calculations only.

Once the quadratic subproblem (A.1) is solved, an inexact line search is performed along the obtained direction $\boldsymbol{p}$. This comprises searching a step size that sufficiently decreases the cost functional. To this end, a generalization of the Wolfe criteria [15] is used in our algorithm. These also demand a sufficient decrease in cost functional line derivative. When the search line crosses constraints, the projection algorithm explained in section 3.3 is applied to bend the search line along the constraint surface. In this way the search direction can become slightly altered compared to the initial search direction. The art of a good line search algorithm is finding a step length that obeys the Wolfe conditions with as few cost functional evaluations as possible. Advanced interpolation strategies can be applied that use former cost functional and gradient information to search the lowest value along the line. In our algorithm a line search strategy developed by More and Thuente [20] is adapted to account for the projection of unfeasible control variable combinations onto the feasible set.

References

[1] Kukushkin A, Pacher H, Kotov V, Pacher G and Reiter D 2011 *Fusion Engineering and Design* **86** 2865–2873 ISSN 0920-3796 URL http://www.sciencedirect.com/science/article/pii/S092037961100514X

[2] Kotschenreuther M, Valanju P M, Mahajan S M and Wiley J C 2007 *Physics of Plasmas (1994-present)* **14** URL http://scitation.aip.org/content/aip/journal/pop/14/7/10.1063/1.2739422

[3] Reiter D, Baelmans M and Börner P 2005 *Fusion Science and Technology* **47** 172–186

[4] Dekeyser W, Reiter D and Baelmans M 2012 *Contrib. Plasma Phys.* **52** 544–549 ISSN 1521-3986 URL http://dx.doi.org/10.1002/ctpp.201210047

[5] Dekeyser W, Reiter D and Baelmans M 2014 *Nuclear Fusion* **54** 073022 ISSN 0029-5515 URL http://stacks.iop.org/0029-5515/54/i=7/a=073022

[6] Romanelli F, Laxåback M and on behalf of the JET EFDA Contributors 2011 *Nuclear Fusion* **51** 094008 ISSN 0029-5515 URL http://stacks.iop.org/0029-5515/51/i=9/a=094008
[7] Shafranov V D 1966 *Reviews of Plasma Physics* **2** 103
[8] Dnestrovskii Y N and Kostomarov D P 1986 Controlled fusion and numerical simulation *Springer Series in Computational Physics* (Springer Berlin Heidelberg) pp 1–28
[9] Baelmans M, Blommaert M, De Schutter J, Dekeyser W and Reiter D *Plasma Physics and Controlled Fusion* Accepted for publication
[10] Rensink M E, Lodestro L, Porter G D, Rognlien T D and Coster D P 1998 *Contrib. Plasma Phys.* **38** 325–330 ISSN 1521-3986 URL http://dx.doi.org/10.1002/ctpp.2150380149
[11] Marchand R and Dumberry M 1996 *Computer Physics Communications* **96** 232–246 ISSN 0010-4655 URL http://www.sciencedirect.com/science/article/pii/0010465596000525
[12] Baelmans M, Börner P, Dekeyser W and Reiter D 2011 *Nuclear Fusion* **51** 083023 ISSN 0029-5515 URL http://stacks.iop.org/0029-5515/51/i=8/a=083023
[13] Hazra S and Schulz V 2004 **44** 457–472 ISSN 0006-3835
[14] Dekeyser W, Reiter D and Baelmans M 2014 *Int. J. Computational Science and Engineering* **9** 397–407
[15] Nocedal J and Wright S 2006 *Numerical Optimization* (Springer)
[16] Viola B, Frigione D, Belo P, Groth M, Kempenaars M, Kruezi U, Marsen S, Stamp M and contributors J E 2013 Study of the effect of the outer-strike point location on the divertor neutral pressure in JET-ILW using EDGE2D/EIRENE *40th European Physical Society Conference on Plasma Physics*
[17] Braginskii S I 1965 *Reviews of Plasma Physics* **1** 205
[18] Coster D P, Bonnin X, Braams B, Reiter D, Schneider R and the ASDEX Upgrade Team 2004 *Physica Scripta* **2004** 7–13 ISSN 1402-4896 URL http://stacks.iop.org/1402-4896/2004/i=T108/a=001
[19] Reiter D 2009 *The Eirene Code User Manual, including: B2-EIRENE interface* URL www.eirene.de
[20] Moré J J and Thuente D J 1994 *ACM Trans. Math. Softw.* **20** 286–307